2024 IEEE International Conference on Robotics and Automation (ICRA 2024)
May 13-17, 2024. Yokohama, Japan

A Study of Force-Free Control Framework for Industrial Manipulator Tasks Based on High-Pass Filter

Guanwei He[1], Guodong Feng[1], and Beichen Ding[2*]

Abstract— **Force-free control (FFC) allows for flexible manipulator motion in response to external forces, making it a vital component of human-robot interaction (HRI). Manual intervention may cause uneven forces on the manipulator or frequencies close to the natural frequency, and mechanical resonance can occur due to the inertia of the manipulator and adjustable equivalent stiffness of the controller. This paper proposes an FFC approach for industrial manipulators using a six-axis force/torque sensor (F/T sensor), implemented through a three-layer control architecture, consisting of motion control layer, Admittance Control layer and force decoupling layer. To mitigate the effects of mechanical resonance, a high-pass filter (HPF) is integrated with the F/T sensor and its impact is investigated. Experimental validation is conducted using both a simulation model and an industrial manipulator. Test results indicate that the proposed FFC architecture enables the manipulator not only to interact smoothly with external forces, but also to distinguish load forces at different frequencies and potentially address the issue of mechanical resonance between the manipulator and the applied load forces.**

I. Introduction

To achieve demand trajectory tracking of a manipulator and accomplish HRI tasks, direct teaching has gained popularity over other methods, e.g., teaching box programing and offline teaching, due to its intuitive operation and high efficiency of trajectory generating [1]. FFC technique enables inexperienced staff members to smoothly operate the manipulator, which is crucial for direct teaching. The FFC can be classified into three types according to sensor usage:

1) without any force or torque (F/T) sensor (WOFTS);
2) with joint torque sensor (WJTS);
3) with multi-axis F/T sensor at the end-effector (WF/TS).

The first two approaches heavily rely on the accurate modelling of the manipulator's coupled dynamics. FFC without force or torque sensor in [2] compensates for this by calculating the gravity and friction terms in the dynamics. In [3]-[5], current sensors are employed to reflect motor output torque. [6]-[7] introduce generalized momentum observer to estimate external forces, aiding in dynamics estimation in sensor-less scenarios. Joint torque sensor [8]-[10] enables more precise dynamics and force control by feeding back each joint torque, bringing about more practical FFC. However, this method not only costs a lot but also imposes stringent requirements on the mechanical and electronic design of the joints. In [1], [11]-[12], FFC with F/T sensor at the end-effector directly senses external forces and enables direct teaching tasks in conjunction with a position controller. Table I presents an overview of the advantages and disadvantages associated with these three approaches.

TABLE I. Merits and Demerits of Different FFC Approaches

	(a) WOFTS	(b) WJTS	(c) WF/TS
Contact region that responses to external force	All over manipulator	All over manipulator	End-effector only
Required manipulator control mode	Torque input mode	Torque input mode	Position input mode
Complexity of deploying on an existing manipulator	With Torque input mode: simple; Without torque input mode: hard.	Hard.	Simple.
Economic cost	Low	High	Medium

Impedance Control and Admittance Control are widely used in HRI scenarios, including FFC approaches. In Impedance Control, the manipulator is regarded as an admittance, and vice versa for Admittance Control [13]. As a result, WOFTS and WJTS are associated with Impedance Control, and Admittance Control always copes with FFC with multi-axis F/T sensor. Considering practical situation, the former requires torque input to the plant, while the latter only necessitates position input. However, typical industrial manipulators only support velocity/position input mode on low-level joint controllers [14], making it challenging to apply Impedance Control.

Transmission mechanisms can result in finite stiffness of servo systems [15], and the adjustable admittance and in conjunction with PID controllers gives a relatively certain system stiffness k_e. The inertial properties of a manipulator can be regarded as an equivalent mass m_e. Due to elaborate industrial operations, the loading force manifests itself across a broad spectrum of frequencies. This elevates the likelihood of manipulator experiencing resonance, wherein its equivalent natural frequency $\omega_e = \sqrt{k_e / m_e}$ coincides with the frequency of loading forces. This introduces a heightened level of uncertainty and uncontrollability to an engineering system, probably resulting in severe malfunctions and considerable damage. Therefore, the system inertia needs to be carefully analyzed accompanied by setting controller parameters to prevent mechanical resonance between load forces and manipulator to mitigate operational instability.

[1] School of Intelligent Systems Engineering, Shenzhen Campus of Sun Yat-sen University, Shenzhen, China.
[2] School of Advanced Manufacturing, Shenzhen Campus of Sun Yat-sen University, Shenzhen, China.
[*] Corresponding Author: dingbch@mail.sysu.edu.cn.

This paper proposes an FFC method for industrial manipulators facing resonance. The main contributions of this paper include:

1) A novel three-layer FFC framework is successfully implemented even if the external force is slight.

2) The framework is readily implemented on existing systems, and suitable for both torque-input-support and position-input-support industrial manipulators.

3) A force decoupling layer is introduced, which allows for distinguishing alternating component (AC) and direct component (DC) forces.

II. Experiment Setup

A. Hardware

The hardware system consists of an industrial manipulator and a six-axis F/T sensor shown in Table II. The F/T sensor is bolted at the end-effector of the manipulator.

TABLE II. HARDWARE COMPONENTS

Components	Model	Key Parameters
Manipulator	Han's Elfin 3	Weight: 18 kg; Payload: 3kg; Max speed of end-effector: 2m/s; Degree of Freedom (DoF): 6; Repeatability: ±0.02mm.
F/T sensor	Kunwei KWR75B	Force Range (x, y, z): 200N; Torque Range (x, y, z): 8N·m; Sampling Frequency: 1000Hz; Resolution: 0.03% Full Scale; Accuracy: 0.5% Full Scale.

B. Software Framework

The software system is based on Robot Operating System (ROS) [16] shown in Fig. 1.

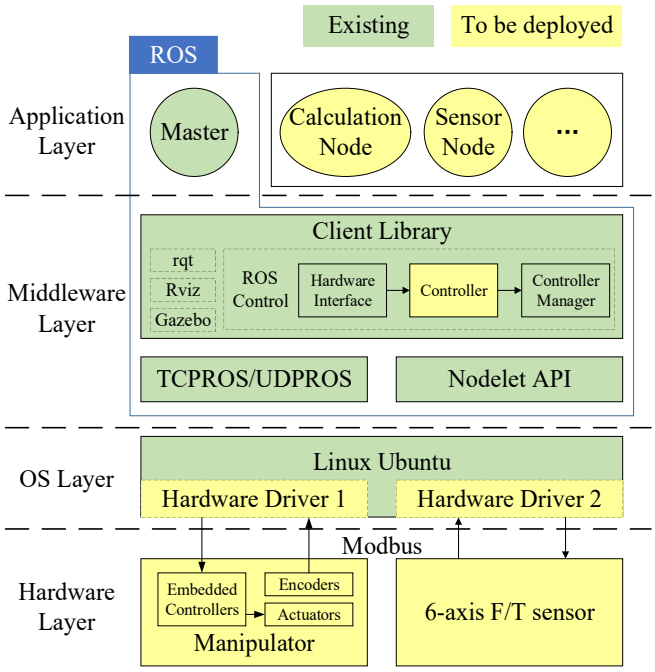

Figure 1. Software framework based on ROS

Noteworthily, minimal modifications have been made to the software framework and hardware system, allowing for rapid deployment on existing manipulators. Elfin 3 provides hardware_interface::EffortJointInterface, i.e. torque input mode，receiving torque input with a maximum frequency of 10 Hz. Leveraging this capability, the position controller is regenerated, even though its necessity is relatively lower, especially for manipulators that only provide position input.

III. Modelling

This section develops a detailed model of our study, including mathematical model and simulation model. Vectors or matrices are represented by bold symbols in this paper.

A. Kinematics

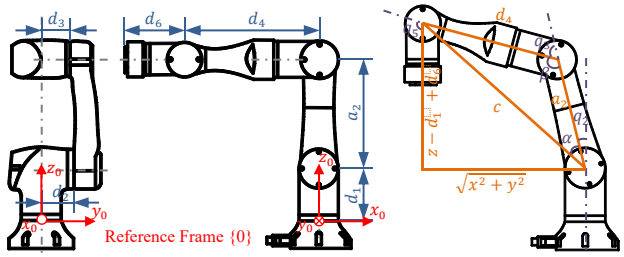

Figure 2. Kinematics of Elfin 3 manipulator

The vector of joint variables is defined as $\boldsymbol{q} = [q_1, \ldots, q_n]^T$, where $\boldsymbol{q} \in \mathbb{R}^n$ with $n = 6$. To obtain forward kinematics, standard Denavit-Hartenberg (D-H) parameters are shown in Table III.

TABLE III. LINK PARAMETERS OF ELFIN 3 MANIPULATOR

i	a_i	α_i	d_i	q_i
1	0	$-\frac{\pi}{2}$	d_1	q_1
2	a_2	π	d_2	$q_2 - \frac{\pi}{2}$
3	0	$-\frac{\pi}{2}$	d_3	$q_3 - \frac{\pi}{2}$
4	0	$\frac{\pi}{2}$	d_4	q_4
5	0	$-\frac{\pi}{2}$	0	q_5
6	0	0	d_6	q_6

The transformation that defines frame $\{i\}$ relative to frame $\{i\text{-}1\}$, namely ${}^{i-1}_{i}T$, is constructed by [17]:

$$ {}^{i-1}_{i}\boldsymbol{T} = \begin{bmatrix} cq_i & -sq_i c\alpha_i & sq_i s\alpha_i & a_i cq_i \\ sq_i & cq_i c\alpha_i & -cq_i s\alpha_i & a_i sq_i \\ 0 & s\alpha_i & c\alpha_i & d_i \\ 0 & 0 & 0 & 1 \end{bmatrix} \quad (1) $$

where cq_i is shorthand for $\cos q_i$, sq_i for $\sin q_i$, and so on.

Then, the forward kinematics, i.e. the transformation that relates frame $\{n\}$ to frame $\{0\}$, is calculated by:

$$ {}^{0}_{n}\boldsymbol{T} = {}^{0}_{1}\boldsymbol{T}\,{}^{1}_{2}\boldsymbol{T}\ldots{}^{n-1}_{n}\boldsymbol{T} = \begin{bmatrix} {}^{0}_{n}\boldsymbol{R} & \boldsymbol{P} \\ 0 & 1 \end{bmatrix} \tag{2} $$

where ${}^{0}_{n}\boldsymbol{R} \in \mathbb{R}^{3\times3}$ is the rotation matrix representing the orientation of frame $\{n\}$ in frame $\{0\}$, and $\boldsymbol{P} \in \mathbb{R}^{3}$ is the Cartesian coordinates relative to frame $\{0\}$.

The position of the end-effector is defined by $\boldsymbol{P} = [x, y, z]^T$ in Cartesian space, where x, y, z are the position coordinates relative to the reference frame $\{0\}$. The respective orientation coordinates are expressed by Z-Y-X Euler Angles. Let's say:

$$ {}^{0}_{n}\boldsymbol{R}_{ZYX} = \boldsymbol{R}_z(q_1)\boldsymbol{R}_Y(\pi)\boldsymbol{R}_X(0) \tag{3} $$

Geometric solution is used to obtain inverse kinematics, where Law of Cosines is the core:

$$ c = \sqrt{x^2 + y^2 + \left(z - d_1 + d_6\right)^2} \tag{4} $$

$$ \alpha = \arccos\left(\frac{c^2 + a_2^2 - d_4^2}{2a_2 c}\right) \tag{5} $$

$$ \beta = \arccos\left(\frac{a_2^2 + d_4^2 - c^2}{2a_2 d_4}\right) \tag{6} $$

Combining Fig. 2, inverse kinematics is given:

$$ \begin{cases} q_1 = \operatorname{atan2}(y, x) \\ q_2 = \operatorname{atan2}\left(\dfrac{\sqrt{x^2 + y^2}}{z - d_1 + d_6}\right) - \alpha \\ q_3 = \pi - \beta \\ q_4 = 0 \\ q_5 = \pi - q_2 - q_3 \\ q_6 = 0 \end{cases} \tag{7} $$

B. Dynamics

The dynamics of manipulator is modelled by:

$$ \boldsymbol{M}(\ddot{\boldsymbol{q}}) + \boldsymbol{C}(\boldsymbol{q}, \dot{\boldsymbol{q}})\dot{\boldsymbol{q}} + \boldsymbol{g}(\boldsymbol{q}) + \boldsymbol{\tau}_f = \boldsymbol{\tau}_c + \boldsymbol{\tau}_{ext} \tag{8} $$

where $\boldsymbol{M}(\boldsymbol{q})$ is the inertia matrix, $\boldsymbol{C}(\boldsymbol{q},\dot{\boldsymbol{q}})\dot{\boldsymbol{q}}$ is the vector of Coriolis torques, $\boldsymbol{g}(\boldsymbol{q})$ is the gravitational torques, $\boldsymbol{\tau}_f$ is the vector of the friction torques, $\boldsymbol{\tau}_c$ is the controlled torques provided by joint motors, and $\boldsymbol{\tau}_{ext}$ is the joint torque resulting from external forces.

The inclusion of the inertia matrix term and Coriolis term is omitted in this study, considering the intricate coupling and computational complexity involved. Alternatively, gravitational torques and friction torques are computed to provide compensation for motion control. The friction torque $\tau_{fi} \in \boldsymbol{\tau}_f$, $i = 1, \ldots, n$ is modelled by [18]:

$$ \tau_{fi} = \begin{cases} F_{ci} & for \quad f_v \geq F_{ci} \\ f_v \dot{q}_i & for \quad |f_v \dot{q}_i| < F_{ci} \\ -F_{ci} & for \quad f_v \dot{q}_i \leq -F_{ci} \end{cases} \tag{9} $$

where F_{ci} is the Coulomb friction torque at joint i, f_v is a static friction coefficient which is relatively large.

C. Simulation Model

The simulation model is built in MATLAB®/Simulink®, and the plant model is built using Simscape Multibody, as shown in Fig. 3.

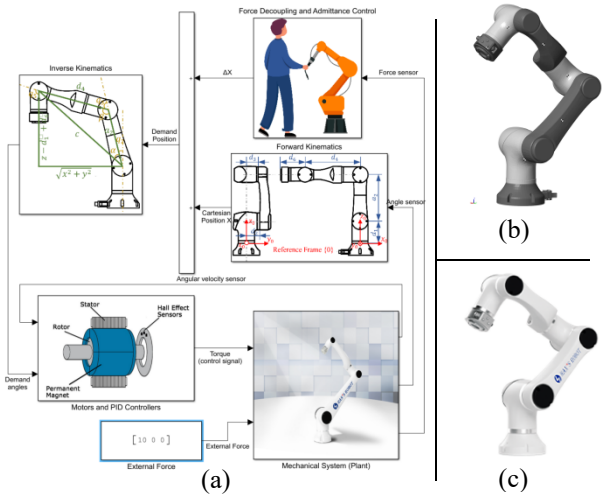

Figure 3. Simulation model. (a) Simulink diagram. (b) Simulation view in MATLAB. (c) Real manipulator.

IV. Control Architecture

In this section, a three-layer control architecture is presented, as shown in Fig. 4. The outer force decoupling layer is responsible for decoupling the external force sensed into DC and AC forces. Then, the middle Admittance Control layer is responsible for mapping those forces to the target position of the manipulator. Finally, the inner motion control layer achieves precise position control.

A. Motion Control Layer

In this layer, a position controller is implemented. PID controllers are utilized for each joint, while compensating for gravitational and friction torques. To enhance the response, a slight velocity feedforward mechanism is incorporated. The aforementioned torques are summed together to form a control signal received by each joint.

B. Admittance Control Layer

This layer receives the processed DC force $\boldsymbol{F}_{DC} = [F_{DC\text{-}x}, F_{DC\text{-}y}, F_{DC\text{-}z}]^{\mathrm{T}}$ and AC Cartesian position $\Delta\boldsymbol{P}_{AC} = [\Delta P_{AC\text{-}x}, \Delta P_{AC\text{-}y}, \Delta P_{AC\text{-}z}]^{\mathrm{T}}$ signals and calculates demand positions.

Admittance Control connects demand Cartesian position increment to external force:

$$ \Delta\boldsymbol{P}_{\boldsymbol{DC}} = \boldsymbol{K}_{adm}^{-1}\boldsymbol{F}_{\mathrm{DC}} = [\Delta P_{DC-x}, \Delta P_{DC-y}, \Delta P_{DC-z}]^T \tag{10} $$

where admittance $\boldsymbol{K}_{adm} = \operatorname{diag}(k_{adm\text{-}x}, k_{adm\text{-}y}, k_{adm\text{-}z}) \in \mathbb{R}^{3\times3}$. Together with feedback position $\boldsymbol{P}_{fb}$, the demand Cartesian position is calculated by:

$$ \boldsymbol{P}_d = \boldsymbol{P}_{fb} + \Delta\boldsymbol{P}_{\boldsymbol{DC}} + \Delta\boldsymbol{P}_{\boldsymbol{AC}} = [P_{d-x}, P_{d-y}, P_{d-z}]^T \tag{11} $$

which is converted into joint space demand angels $\boldsymbol{q}_d$ by inverse kinematics.

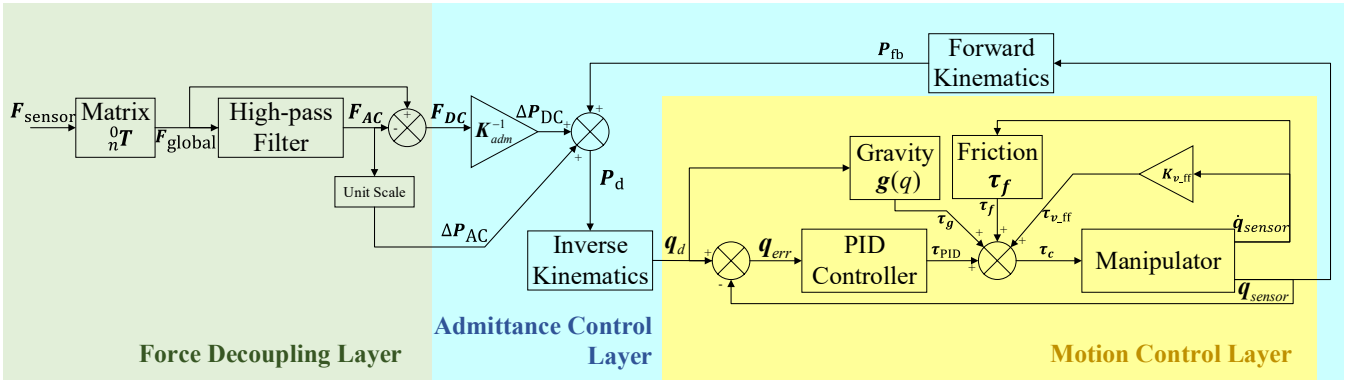

Figure 4. The three-layer control architecture

C. Force Decoupling Layer

This layer processes data from F/T sensor $\boldsymbol{F}_{\text{sensor}}$ into DC force $\boldsymbol{F}_{DC}$ and AC position $\Delta\boldsymbol{P}_{AC}$.

Force signals are $\boldsymbol{F}_{\text{sensor}} \in \mathbb{R}^3$ relative to frame {6}, which need to be transformed into global force signals relative to frame {0}:

$$\boldsymbol{F}_{\text{global}} = {}^{0}_{n}\boldsymbol{R}\boldsymbol{F}_{\text{sensor}} = \begin{bmatrix} F_x & F_y & F_z \end{bmatrix}^T \tag{12}$$

Forces at difference frequencies are decoupled using first-order HPF $\boldsymbol{H}(\boldsymbol{s})$:

$$\boldsymbol{H}(\boldsymbol{s}) = diag\left(\frac{\omega_{c1}}{s_x + \omega_{c1}} \quad \frac{\omega_{c2}}{s_y + \omega_{c2}} \quad \frac{\omega_{c3}}{s_z + \omega_{c3}} \right) \tag{13}$$

$$\boldsymbol{F}_{\text{AC}}(\boldsymbol{s}) = \boldsymbol{H}(\boldsymbol{s})\boldsymbol{F}_{\text{global}}(\boldsymbol{s}) \tag{14}$$

$$\boldsymbol{F}_{\text{DC}} = \boldsymbol{F}_{\text{global}} - \boldsymbol{F}_{\text{AC}} \tag{15}$$

where Laplacian differential operators s_x, s_y, $s_z \in \boldsymbol{s}$ and ω_{c1}, ω_{c2}, ω_{c3} are cut-off angular frequencies. Unit scale $\boldsymbol{K_{us}} = \text{diag}(k_{us\text{-}x}, k_{us\text{-}y}, k_{us\text{-}z}) \in \mathbb{R}^{3\times3}$ are relatively small proportional to make sure $\Delta\boldsymbol{P}_{AC}$ is in a reasonable range and they are not adjustable.

V. Experiment and Evaluation

Experiments are carried out to explore the effectiveness of Admittance Control and the ability of the proposed framework to distinguish between DC and AC forces.

A. Performance of Admittance Control Layer

As shown in Fig. 5(a), constant force along y_0 axis is applied to the end-effector by fixed pulley and hanging weight $m = 710g$. The weight is released at $t = 1s$. This setup aims to generate a DC dominant motion. Experiments of the proposed architecture under different admittance values are carried out. And a widely-used FFC framework [2] is utilized for the comparative experiment. Results are shown in Fig. 6.

For each curve in Fig. 6, displacement increases linearly with time under constant force, i.e. the increment of displacement is directly proportional to the external force. In our method, through adjusting Admittance k_y, the same force leads to different displacement of end-effector. Determined by admittance and control signal frequency, the slopes calculated with least squares method are 37.5 mm/s, 48.3 mm/s and 60.2 mm/s when $1/k_y$ is 0.6 mm/N, 0.8 mm/N, and 1.0 mm/N respectively. Test results indicates that Admittance Control is effective in regulating HRI performance, and flexibility grows with the reciprocal of admittance.

Compared to the comparative experiment, our architecture produces a larger displacement under the same force, indicating that our architecture is more sensitive to external forces and exhibits better FFC performances. Additionally, our method allows for adjusting the sensitivity to external forces by modifying the admittance values. Furthermore, the comparative method requires high precision in compensating for friction and gravitational torques, usually involving a cumbersome parameter identification to achieve better FFC performance, while our method avoids this laborious process.

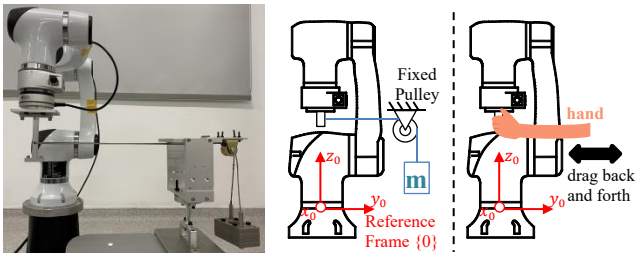

Figure 5. Force applied to the end-effector. (a) Constant force. (b) Reciprocating force.

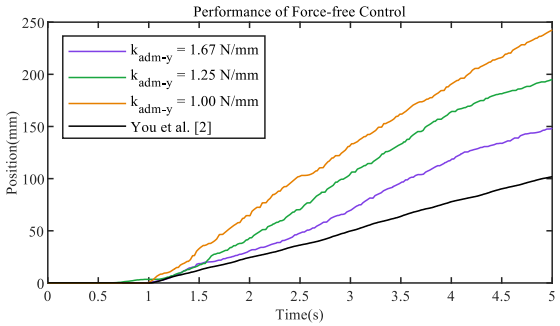

Figure 6. Performance of Force-free Control

B. Performance of Force Decoupling Layer

Constant force is applied as Fig. 5(a) shows. The hanging weight is gently released at $t = 1s$. The sensed force from F/T

sensor and the Cartesian position of the end-effector are shown in Fig. 7.

Regarding Fig. 7(a), the non-zero force at the initial stage may stem from rope tension. The magnitude of the $F_{AC\text{-}y}$ after passing through the HPF is relatively small, and the DC force $F_{DC\text{-}y}$ is approximately equivalent to the original force F_y in numerical terms, with a slight phase lag observed. In this scenario, $\Delta P_{DC\text{-}y}$ predominates in the Admittance Control layer's summation while $\Delta P_{AC\text{-}y}$ can be neglected. As a result, the demand Cartesian position P_d is primarily determined by the force within the DC pathway and the feedback Cartesian position gradually increases approximately in a linear manner as shown in Fig. 7(b). Test results also indicate that the constant force component remains at a low frequency, while the filter effectively removes high-frequency noise.

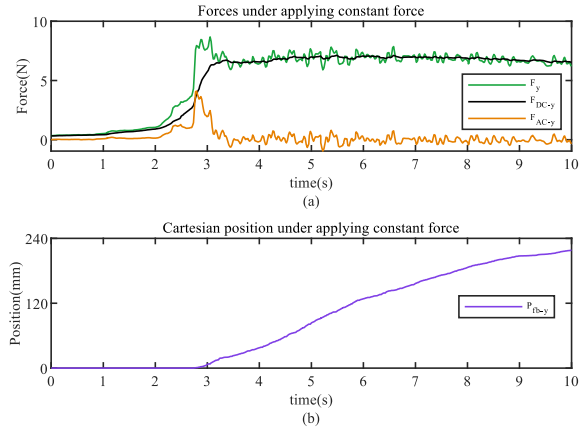

Figure 7. Performance of force decoupling layer when applying a constant force at $k_y = 1.67\ N/mm$. (a) Original force, DC force and AC force data y_0 axis. (b) Cartesian position data along y_0 axis.

As Fig. 5(b) shows, a reciprocating force is exerted when the end-effector is manually dragged back and forth by a human hand. The cut-off frequency of the HPF is 0.5 Hz. Results are shown in Fig. 8.

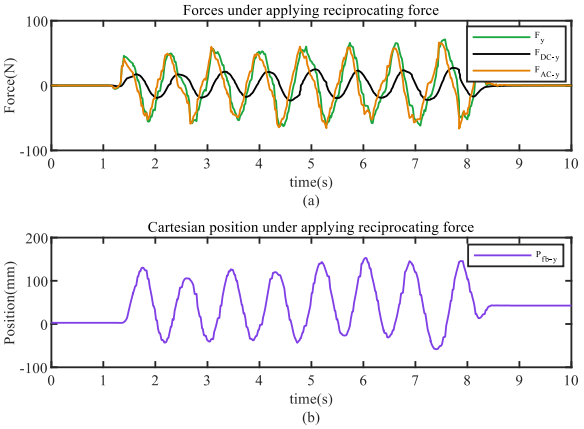

Figure 8. Performance of force decoupling layer when applying a reciprocating force. (a) Original force, DC force and AC force data y_0 axis. (b) Cartesian position data along y_0 axis.

In Fig. 8, it takes around 7.2 seconds to accomplish 8 periods of reciprocating motion, i.e. alternating frequency of F_y is about 1.11 Hz. The input force signal F_y is mainly an alternating signal (AC dominant motion). Therefore, the AC signal $F_{AC\text{-}y}$ that passes through the HPF retains most of the characteristics of the original signal F_y, while $F_{DC\text{-}y}$ is relatively small. From Fig. 8(a), the amplitude of original force F_y and AC force $F_{AC\text{-}y}$ is close, while $F_{AC\text{-}y}$ is slightly ahead in phase compared to F_y. In this situation, the variations of the demand signal P_d primarily stem from the AC channel's $\Delta P_{AC\text{-}y}$.

The experimental results demonstrate that the proposed framework is capable of distinguishing and extracting forces at specific frequencies and responding accordingly. By adjusting the cut-off frequency of the HPF within the approximate range of the daily operational scope and equivalent natural oscillation frequency, it is expected to mitigate the occurrence of mechanical resonance phenomena.

C. Frequency Domain Analysis

Representing the system as a transfer function (TF) form facilitates the analysis of its performance, and one-dimensional motion along y-axis is analyzed as an exemplification. The TF of the force decoupling layer is:

$$G_{fdl}(s) = \frac{k_{us-y}s}{s+\omega_{c2}} + \frac{\omega_{c2}}{(s+\omega_{c2})k_{adm-y}} \tag{16}$$

The PID controller expressed by TF is:

$$G_{PID}(s) = \frac{K_d s^2 + K_p s + K_i}{s} \tag{17}$$

The kinematics are independent of time and consist of numerous trigonometric functions, making it challenging to express the input-output relationship using TFs. However, using linearization techniques such as $sin\ \theta \approx \theta, cos\ \theta \approx 1$ in specific geometric positions, the forward kinematics can be simplified into a proportional term $G_{for}(s) = k_{kine}$. Consequently, the inverse kinematics $G_{inv}(s)$ is the reciprocal of $G_{for}(s)$.

During the experiment, it was observed that near the steady state the manipulator exhibited spring-damping characteristics:

$$G_{\text{mani}}(s) = \frac{k_{\text{mani}}\omega_n^2}{s^2 + 2\xi\omega_n s + \omega_n^2} \tag{18}$$

where the input is motor torque (calculated from current), the output is angular position, ξ is the damping factor, ω_n is the natural frequency of oscillation, and k_{mani} is the gain.

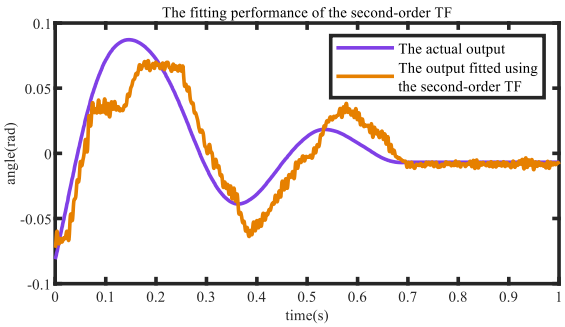

Figure 9. The fitting performance of the second-order TF.

To obtain the manipulator's TF, a portion of the motion signal from the 5th joint is collected. A second-order TF is used to fit the plant as shown in Fig. 9, and exhibits a certain degree of approximation to the actual system. The fitting error may arise from nonlinear factors such as frictional forces.

Then the open-loop TF $G_{ol}(s)$ corresponding to $P_{d\text{-}y}$ as the output and F_y as the input is expressed by:

$$G_{ol}(s) = G_{fdl}(s)G_{inv}(s)G_{PID}(s)G_{\text{mani}}(s)G_{for}(s) \quad (19)$$

To validate the impact of both admittance and HPF cut-off frequency, magnitudes of Bode Diagram is plotted in Fig. 10.

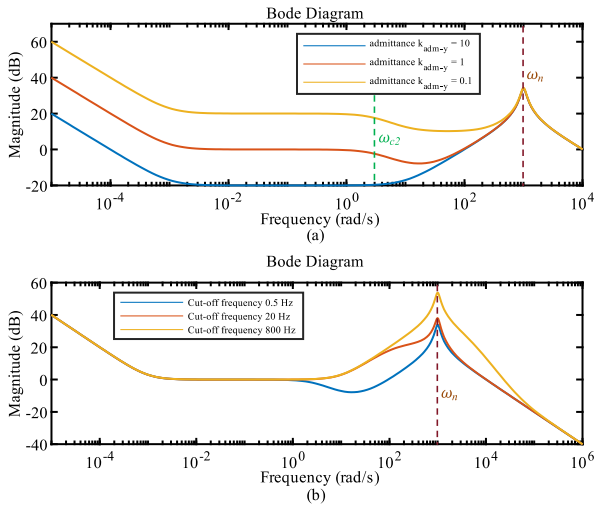

Figure 10. Bode diagram. (a) Performance of admittance. (b) Performance of cut-off frequency

Three different admittance values are respectively employed to plot magnitude curves in Fig. 10(a). As the admittance decreases, the magnitude increases at lower frequencies, while it remains unchanged at higher frequencies. Fig. 10(b) demonstrates the magnitude characteristics at different cut-off frequencies. Within the extremely high and low frequency range, adjusting ω_{c2} has virtually no impact on the output magnitude. In the vicinity of ω_n, the amplitude increases with the increase in the cut-off frequency.

Test results indicate that the admittance influences the magnitude of the system's output when subjected to low-frequency signal inputs, while ω_{c2} affects the amplitude of the system's output when subjected to signal inputs near ω_n.

D. Elimination of Phase Distortion

The utilization of a zero-phase filter involves processing the data sequence in both the forward and reverse directions, aiming to reduce phase delay to the level of calculation delay, thereby minimizing the overall latency [19]. The function *filtfilt*() is available in Python and MATLAB to achieve a zero-phase filter. It is worth noting that there may be a slight difference in the performance between a real-time zero-phase filter and an off-line zero-phase filter, with the former showing a slightly inferior latency. The differential effects of conventional filtering and zero-phase filtering on data processing are documented in the curve presented in Fig. 11.

Experimental findings indicate a notable impact of zero-phase filtering in adjusting latency. As Fig. 11(a) shows, utilizing the zero-phase filter with the constant force enables effective improvement of phase lag issues, resulting in a smoother curve while maintaining nearly unchanged amplitude. This is helpful in accelerating response speed. However, applying the zero-phase filter to the alternating force in Fig. 11(b) not only reduces the amplitude but also eliminates the characteristic of phase advance, which is undesirable for the system. This provides insights for improving the force decoupling layer. It is preferable to use conventional filters when dealing with AC forces, and zero-phase filtering is more effective when handling DC forces.

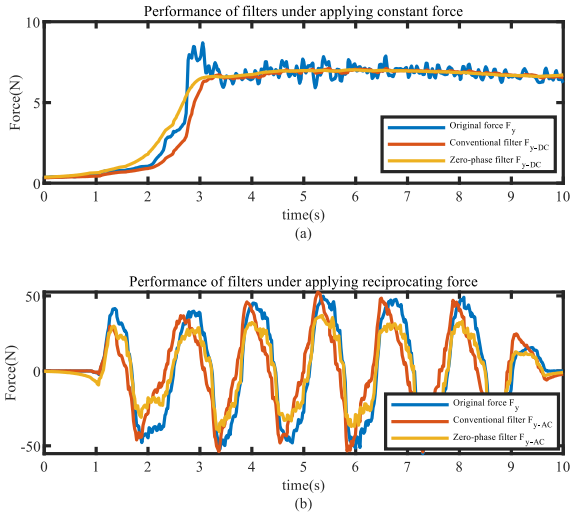

Figure 11. Performance of zero-phase filter. (a) Constant force. (b) Reciprocating force.

VI. Conclusion and Future Work

This research contributes to the field of industrial manipulator control by offering an innovative FFC framework that enhances interactions with external forces and effectively addresses mechanical resonance issues.

Importantly, the experimental results demonstrate the effectiveness of the Admittance Control layer in regulating HRI performance, with flexibility increasing reciprocally with Admittance. Furthermore, the proposed framework successfully distinguishes and extracts forces at specific frequencies, allowing the manipulator to respond accordingly. By adjusting the cut-off frequency of the HPF within the operational range and equivalent natural oscillation frequency, the occurrence of mechanical resonance phenomena is expected to be reduced.

Future work should focus on investigating the impact of forces within the intermediate frequency range between DC forces and AC forces on resonance. Additionally, calculating the equivalent spring and stiffness of the manipulator and conducting system frequency domain analysis would provide valuable insights for further improvements.

Acknowledgment

The authors would like to thank the National Natural Science Foundation of China (52105079).

REFERENCES

[1] L. Huang, J. Yang, S. Ni, B. Wang and H. Zhang, "Research on Robot Teaching for Complex Task," 2020 39th Chinese Control Conference (CCC), Shenyang, China, 2020, pp. 3735-3740, doi: 10.23919/CCC50068.2020.9189538.

[2] Y. You, Y. Zhang, and C. Li, "Force-free control for the direct teaching of robots," Journal of mechanical engineering 50.3 (2014): 10-17.

[3] S. -D. Lee, K. -H. Ahn and J. -B. Song, "Torque control based sensorless hand guiding for direct robot teaching," 2016 IEEE/RSJ International Conference on Intelligent Robots and Systems (IROS), Daejeon, Korea (South), 2016, pp. 745-750, doi: 10.1109/IROS.2016.7759135.

[4] S. Wang, J. Yuan, X. Fu, N. Wang, W. Zhang and P. Xu, "Control and modeling for direct teaching of industrial articulated robotic arms," 2016 IEEE/RSJ International Conference on Intelligent Robots and Systems (IROS), Daejeon, Korea (South), 2016, pp. 923-928, doi: 10.1109/IROS.2016.7759160.

[5] J. Du, J. Yuan, Z. Han and Y. Qian, "Current-Based Direct Teaching for Industrial Manipulator," 2019 IEEE International Conference on Robotics and Biomimetics (ROBIO), Dali, China, 2019, pp. 1647-1652, doi: 10.1109/ROBIO49542.2019.8961867.

[6] A. Wahrburg, E. Morara, G. Cesari, B. Matthias and H. Ding, "Cartesian contact force estimation for robotic manipulators using Kalman filters and the generalized momentum," 2015 IEEE International Conference on Automation Science and Engineering (CASE), Gothenburg, Sweden, 2015, pp. 1230-1235, doi: 10.1109/CoASE.2015.7294266.

[7] M. Capurso, M. M. G. Ardakani, R. Johansson, A. Robertsson and P. Rocco, "Sensorless kinesthetic teaching of robotic manipulators assisted by observer-based force control," 2017 IEEE International Conference on Robotics and Automation (ICRA), Singapore, 2017, pp. 945-950, doi: 10.1109/ICRA.2017.7989115.

[8] S. Goto, N. Nakamura and N. Kyura, "Forcefree control with independent compensation for inertia friction and gravity of industrial articulated robot arm," 2003 IEEE International Conference on Robotics and Automation (Cat. No.03CH37422), Taipei, Taiwan, 2003, pp. 4386-4391 vol.3, doi: 10.1109/ROBOT.2003.1242279.

[9] Albu‐Schäffer, A., Haddadin, S., Ott, C., Stemmer, A., Wimböck, T. and Hirzinger, G. (2007), "The DLR lightweight robot: design and control concepts for robots in human environments", Industrial Robot, Vol. 34 No. 5, pp. 376-385. https://doi.org/10.1108/01439910710774386.

[10] C. Park, Jin Ho Kyung, Hyun Min Do and Taeyong Choi, "Development of direct teaching robot system," 2011 8th International Conference on Ubiquitous Robots and Ambient Intelligence (URAI), Incheon, Korea (South), 2011, pp. 730-732, doi: 10.1109/URAI.2011.6145921.

[11] D. Kushida, M. Nakamura, S. Goto and N. Kyura, "Flexible motion realized by force free control: pull-out-work by articulated robot arm," Proceedings 2001 ICRA. IEEE International Conference on Robotics and Automation (Cat. No.01CH37164), Seoul, Korea (South), 2001, pp. 2747-2752 vol.3, doi: 10.1109/ROBOT.2001.933038.

[12] X. Fu and Y. Li, "Research on the direct teaching method of robot based on admittance control," 2020 12th International Conference on Intelligent Human-Machine Systems and Cybernetics (IHMSC), Hangzhou, China, 2020, pp. 48-52, doi: 10.1109/IHMSC49165.2020.00019.

[13] C. Ott, R. Mukherjee and Y. Nakamura, "Unified Impedance and Admittance Control," 2010 IEEE International Conference on Robotics and Automation, Anchorage, AK, USA, 2010, pp. 554-561, doi: 10.1109/ROBOT.2010.5509861.

[14] E. Mariotti, E. Magrini and A. D. Luca, "Admittance Control for Human-Robot Interaction Using an Industrial Robot Equipped with a F/T Sensor," 2019 International Conference on Robotics and Automation (ICRA), Montreal, QC, Canada, 2019, pp. 6130-6136, doi: 10.1109/ICRA.2019.8793657.

[15] S. N. Vukosavic and M. R. Stojic, "Suppression of torsional oscillations in a high-performance speed servo drive," in IEEE Transactions on Industrial Electronics, vol. 45, no. 1, pp. 108-117, Feb. 1998, doi: 10.1109/41.661311.

[16] Quigley, Morgan. "ROS: an open-source Robot Operating System." IEEE International Conference on Robotics and Automation (2009).

[17] John J. Craig, "Inverse manipulator kinematics" in *Introduction to Robotics Mechanics and Control*, Upper Saddle River, NJ, USA: Pearson Press, 2005.

[18] B. Ding, A. Plummer and P. Iravani, "A Study of a Compliant Hydraulic Actuator for Running Robots," 2018 Global Fluid Power Society PhD Symposium (GFPS), Samara, Russia, 2018, pp. 1-6, doi: 10.1109/GFPS.2018.8472380.

[19] S. R. Powell and P. M. Chau, "A technique for realizing linear phase IIR filters," in IEEE Transactions on Signal Processing, vol. 39, no. 11, pp. 2425-2435, Nov. 1991, doi: 10.1109/78.97998.